Geochemistry Geophysics Geosystems G3
AN ELECTRONIC JOURNAL OF THE EARTH SCIENCES
Published by AGU and the Geochemical Society

Article
Volume 9, Number 8
27 August 2008
Q08014, doi:10.1029/2008GC002021
ISSN: 1525-2027

Aqueous and isotope geochemistry of mineral springs along the southern margin of the Tibetan plateau: Implications for fluid sources and regional degassing of CO_2

Dennis L. Newell
Department of Earth and Planetary Sciences, University of New Mexico, Albuquerque, New Mexico 87131, USA

Now at Hydrology, Geochemistry and Geology Group, Los Alamos National Laboratory, Los Alamos, New Mexico 87545, USA (dnewell@lanl.gov)

Micah J. Jessup
Department of Earth and Planetary Sciences, University of Tennessee, Knoxville, Tennessee 37996, USA

John M. Cottle
NERC Isotope Geosciences Laboratory, Keyworth, Nottingham NG12 5GG, UK

David R. Hilton
Scripps Institution of Oceanography, University of California, San Diego, La Jolla, California 92093, USA

Zachary D. Sharp and Tobias P. Fischer
Department of Earth and Planetary Sciences, University of New Mexico, Albuquerque, New Mexico 87131, USA

[1] Springs issuing from different faults and shear zones along the crest of the Himalayas tap three different levels of crust beneath the Tibetan Plateau. From structurally highest to lowest these are the Tingri Graben, the South Tibetan Detachment System (STDS), and the Ama Drime massif (ADM). The aqueous chemistry reflects water-rock interactions along faults and is consistent with mapped rock types. Major ion chemistry and calculated temperatures indicate that spring waters have circulated to greater depths along the N-S trending faults that bound the Tingri Graben and Ama Drime detachment (ADD) compared to the STDS, suggesting that these structures penetrate to greater depths. Springs have excess CO_2, N_2, He, and CH_4 compared to meteoric water values, implying addition from crustal sources. The $^3He/^4He$ ratios range from 0.018 to 0.063 R_A and are consistent with a crustal source for He. The $\delta^{13}C$ values of dissolved inorganic carbon (DIC) and CO_2 gas range from −5.5 to +3.8‰ and −13.1 to −0.3‰ versus Peedee belemnite, respectively. Sources of carbon are evaluated by calculating isotopic trajectories associated with near-surface effervescence of CO_2. Positive $\delta^{13}C$ values of the Tingri graben and STDS springs are consistent with decarbonation of marine carbonates as the source of CO_2. Negative values for the ADD springs overlap with mantle values but are best explained by metamorphic devolatilization of reduced sedimentary carbon. The $\delta^{15}N$ values of N_2 range from −2.2 to +2.1‰ (versus AIR) and are explained by mixtures of air-derived nitrogen, metamorphic devolatilization of sedimentary nitrogen, and nitrogen from near-surface biogenic processes. CO_2 flux is estimated by scaling from individual springs ($\sim 10^5$ mol a^{-1} per spring) to extensional structures across the southern limit of the Tibetan Plateau and likely contributes between 10^8 and 10^{11} mol a^{-1} (up to 10%) to the global carbon budget.

Components: 11,821 words, 7 figures, 6 tables.

Keywords: Tibetan Plateau; springs; $\delta^{13}C$; $\delta^{15}N$; $^{3}He/^{4}He$; CO_2 flux.

Index Terms: 1034 Geochemistry: Hydrothermal systems (0450, 3017, 3616, 4832, 8135, 8424); 8107 Tectonophysics: Continental neotectonics (8002); 8045 Structural Geology: Role of fluids.

Received 6 March 2008; **Revised** 23 June 2008; **Accepted** 15 July 2008; **Published** 27 August 2008.

Newell, D. L., M. J. Jessup, J. M. Cottle, D. R. Hilton, Z. D. Sharp, and T. P. Fischer (2008), Aqueous and isotope geochemistry of mineral springs along the southern margin of the Tibetan plateau: Implications for fluid sources and regional degassing of CO_2, *Geochem. Geophys. Geosyst.*, *9*, Q08014, doi:10.1029/2008GC002021.

1. Introduction

[2] The Himalayas provide a natural laboratory to study various aspects of collisional orogeny. For example, seismic investigations by the INDEPTH project have identified "bright spots" at midcrustal depths [*Nelson et al.*, 1996], and anomalously low mantle velocities beneath the Tibetan Plateau [*Brown et al.*, 1996]. Using seismic and magnetotelluric techniques, bright spots have been interpreted as partial melt zones, fluid-rich zones, or a mixture of both [*Brown et al.*, 1996; *Kind et al.*, 2002; *Makovsky and Klemperer*, 1999; *Nelson et al.*, 1996; *Wei et al.*, 2001]. Since such interpretations rely on remote sensing techniques with nonunique solutions, debate has centered on the composition of the fluids and their influence on the evolution of the orogen. Beneath the southern Tibetan Plateau and Himalayan crest, for example, bright spots have been interpreted as granitic anatectic melts [*Brown et al.*, 1996]. In contrast, the partial melt zone beneath the northern Tibetan Plateau could include intrusions related to injection of mantle-derived melts [*Tilmann et al.*, 2003; *Turner et al.*, 1993]. In this respect, the presence of seismically slow mantle beneath the north-central Tibetan Plateau would be consistent with the presence of hot, upwelling asthenospheric mantle [*Tilmann et al.*, 2003]. These examples illustrate the ambiguity associated with interpreting the composition of fluids in the Himalayan crust, and any relationship with crustal-scale fault zones or other conduits promoting fluid migration.

[3] A related debate concerns the importance of the Tibetan-Himalayan orogenic flux of CO_2 to the atmosphere, and its climatic impact [*Kerrick and Calderia*, 1993, 1994, 1999; *Kerrick*, 2001]. These studies have relied on estimates of metamorphic decarbonation reactions over the history of the orogen, and have thus focused on paleoclimatic impacts. In light of modern global climate change and its link to atmospheric CO_2 levels, the need to quantify anthropogenic and natural fluxes of carbon to the atmosphere is apparent. However, few studies have made direct carbon flux measurements from non-volcanic tectonic settings [e.g., *Chiodini et al.*, 2004]: indeed, only recently [*Becker et al.*, 2008] have field-based estimates been attempted to quantify the present-day impact of the Tibetan-Himalayan orogen on the global carbon budget.

[4] This study integrates existing structural data from fault zones with geochemical analyses of associated CO_2-rich mineral springs located along the southern margin of the Tibetan Plateau. Our aim is to test if these faults penetrate to sufficient depths to tap the fluid zones found beneath the crust of the plateau. The focus of our approach is to determine if (1) there is a range in fault penetration depths for various extension structures along the southern margin of the Tibetan Plateau, (2) the composition of fluids from various crustal levels is different, and (3) the contribution of this orogen is significant compared to the global carbon budget.

2. Geology of Study Area

[5] The Himalayas extend for >2500 km parallel to the strike of the major structural features that formed in response to the collision of the Indian and Asian plates. The Tibetan Plateau has an average elevation of ~5000 m, and is characterized by crustal east-west extension that is expressed topographically by a network of transform faults and graben [*Fielding*, 1996]. The complexities of the orogen are often grouped into three primary lithotectonic units; from structurally highest to lowest these are the Tibetan Sedimentary Series (TSS), the Greater Himalayan Series (GHS) and the Lesser Himalayan Series (LHS) [*Hodges*, 2000]. The TSS is characterized by passive margin

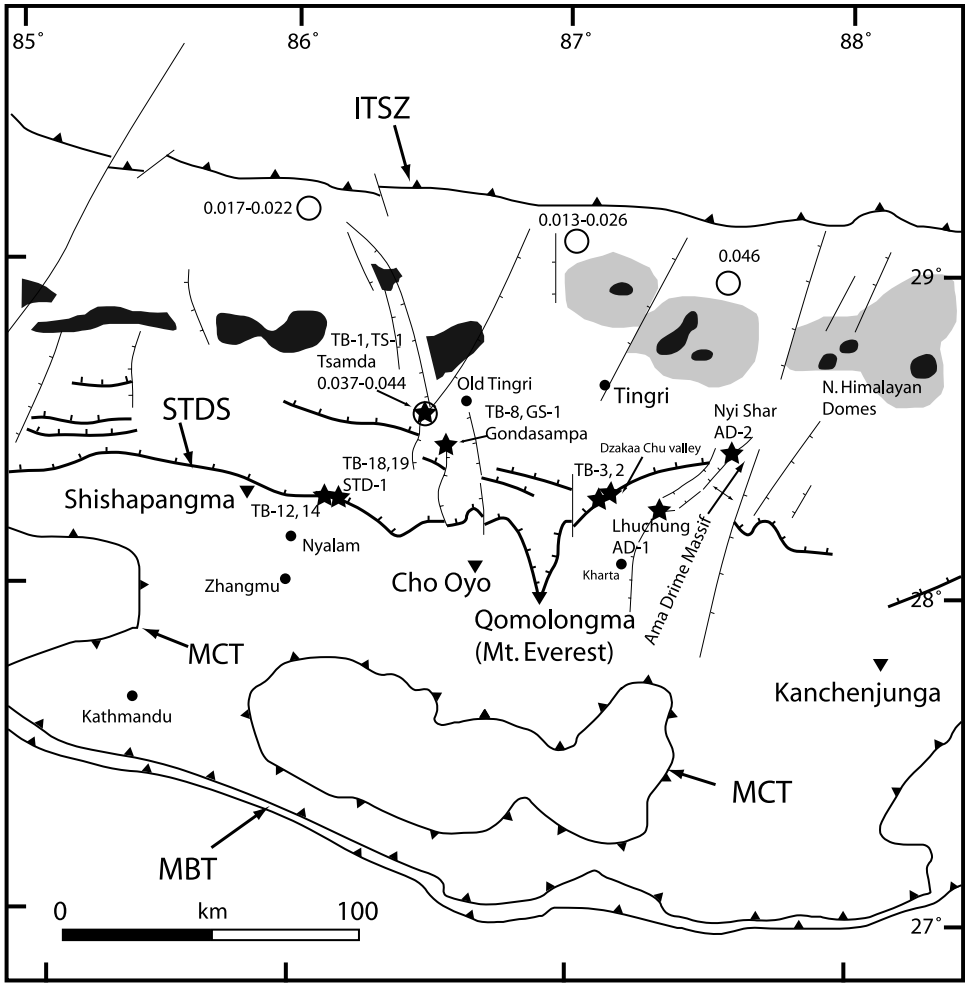

Figure 1. Regional structural map of the Himalaya and Tibetan Plateau containing the study area springs, modified from *Burchfiel et al.* [1992]. North Himalayan domes are shown as leucogranite intrusions (black) surrounded by low-high grade metamorphic rocks (gray shading). Sample locations from this study are shown as stars. Approximate sample locations from *Hoke et al.* [2000] within map area are shown as open circles; associated helium isotopic results are shown (R_A). MBT, Main Boundary Thrust; MCT, Main Central Thrust; STDS, South Tibetan Detachment System; ITSZ, Indus-Tsangpo Suture Zone.

sediments of the Indian Plate, and within the study area these include inter-bedded marine limestones and siliciclastic rocks [*Burchfiel et al.*, 1992]. The GHS includes metasedimentary rocks and Proterozoic granites that were migmatized and injected by anatectic melts during the Miocene [*Searle et al.*, 2003]. The LHS is also composed of metasedimentary rocks and Proterozoic granites that were unaffected by Miocene age metamorphism [*Catlos et al.*, 2002].

[6] Major crustal-scale fault/shear zones bound these units. The South Tibetan Detachment System (STDS) is a low-angle normal fault that is responsible for the juxtaposition of the TSS over the GHS [*Burchfiel et al.*, 1992]. The Main Central Thrust Zone (MCTZ) is a high-strain zone that coincides with an inverted isograd sequence at the base of the GHS and marks the principal transition between the GHS above and LHS below [*Searle et al.*, 2003]. The Main Boundary Fault (MBF) is an active thrust fault that has accommodated deformation as it progressed into the foreland during the evolution of the orogen and marks the base of the LHS [*Hodges*, 2000].

[7] Near the village of Old Tingri, the Tingri graben is ~17 km wide, generally strikes north-south and is filled by an unknown depth of Quaternary outwash from the north side of the Himalayas (Figures 1 and 2). The STDS is exposed on the western limb of this structure and records a deformation history that is very similar to Rongbuk valley and Nyalam [*Jessup et al.*, 2006]. Structurally above the STDS, a section of limestone is present.

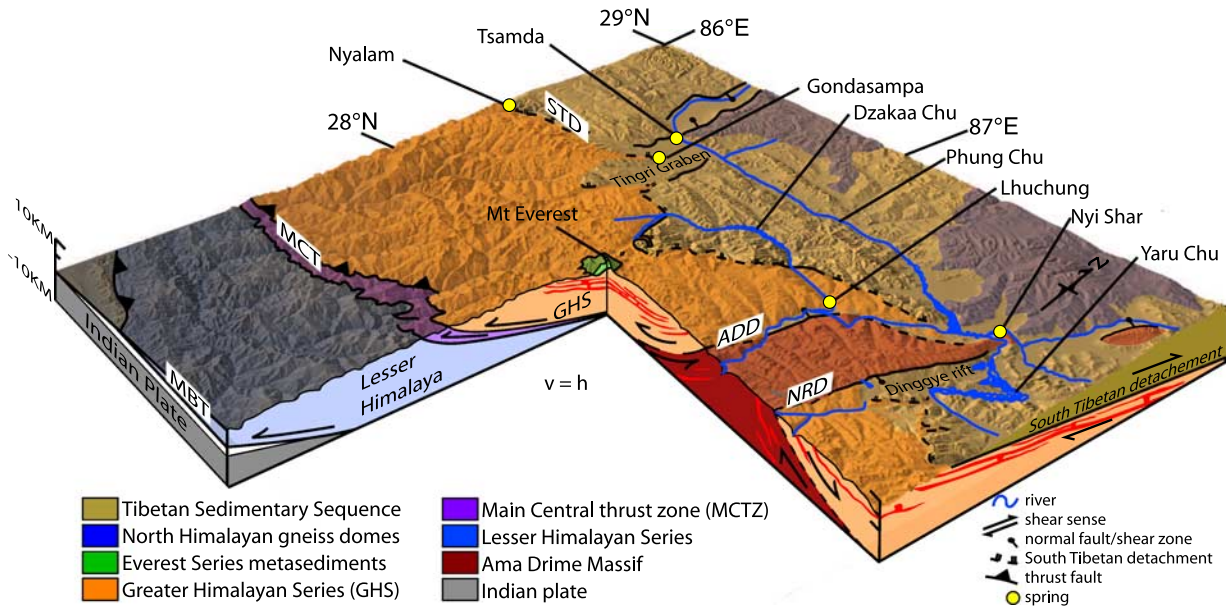

Figure 2. Block diagram after *Jessup et al.* [2008] illustrating the position of the three structural levels with respect to study springs (from Figure 1), major lithotectonic units, and major fault systems. Ama Drime detachment (ADD); Nyönno Ri detachment (NRD).

This limestone is fractured by northeast-striking joint sets ~020–80°E that are filled with laminar calcite veins. Travertine-depositing springs are present with a system of travertine mounds and fissure ridges that strike approximately north-south.

[8] In the study area, the STDS strikes ~ east-west, dips northward 5–30° and displays a range of characteristics in various locations. Near the Friendship Highway by Nyalam, the STDS is defined by a relatively narrow mylonite zone within quartzite, marble and leucogranite that is capped by a discrete brittle fault zone [*Burchfiel et al.*, 1992]. Beneath the mylonite zone, migmatized biotite schist and gneisses record deformation that occurred at high temperatures. A series of marine limestones lies above the detachment. These observations are similar to those observed in Rongbuk valley [*Jessup et al.*, 2006; *Law et al.*, 2004; *Searle et al.*, 2003]. In contrast, farther to the east, just before the Ama Drime Massif (ADM) in the Dzakaa Chu valley, the STDS is characterized by a 1-km-thick distributed shear zone that lacks the low-angle brittle detachment that is common along orogenic strike [*Cottle et al.*, 2007].

[9] The north-south trending, ~30-km-wide, ADM is the most easterly location sampled in this work (Figures 1 and 2). The core of the ADM is composed of the Ama Drime augen gneiss, which is bounded to the east and west by an oppositely dipping shear zones called the Ama Drime Detachment (ADD) and Nyönno Ri Detachment (NRD), respectively [*Jessup et al.*, 2008]. The ADD records top-down-to-the-west movement and the NRD records movement to the east. A progression of deformation mechanisms is recorded by these detachments, from a distributed shear zone to discrete brittle faults that offset Quaternary deposits.

[10] We propose that each of the three main types of extensional faults that comprise this investigation represents a different structural level within the crust of the southern margin of the Tibetan Plateau (Figure 2). Because the faults within the Tingri graben truncate the STDS, as documented in many other sections of the Tibetan Plateau [*Hurtado et al.*, 2001], we interpret it to represent a younger and shallower crustal level than the STDS. The ADM displaces the STDS and, therefore, it has been proposed that the ADD and NRD are younger [*Cottle et al.*, 2007; *Jessup et al.*, 2008]. Since the ADM is located in the footwall of the ADD and NRD, it represents a structurally lower section than the surrounding GHS (Figure 2). We refer to the Tingri graben, the STDS, and the ADM as the highest, intermediate, and lowest structural levels, respectively (Figure 2).

3. Mineral Springs

3.1. Tingri Graben (Highest Structural Level)

[11] Travertine deposits are found along a network of north-south trending normal faults that define

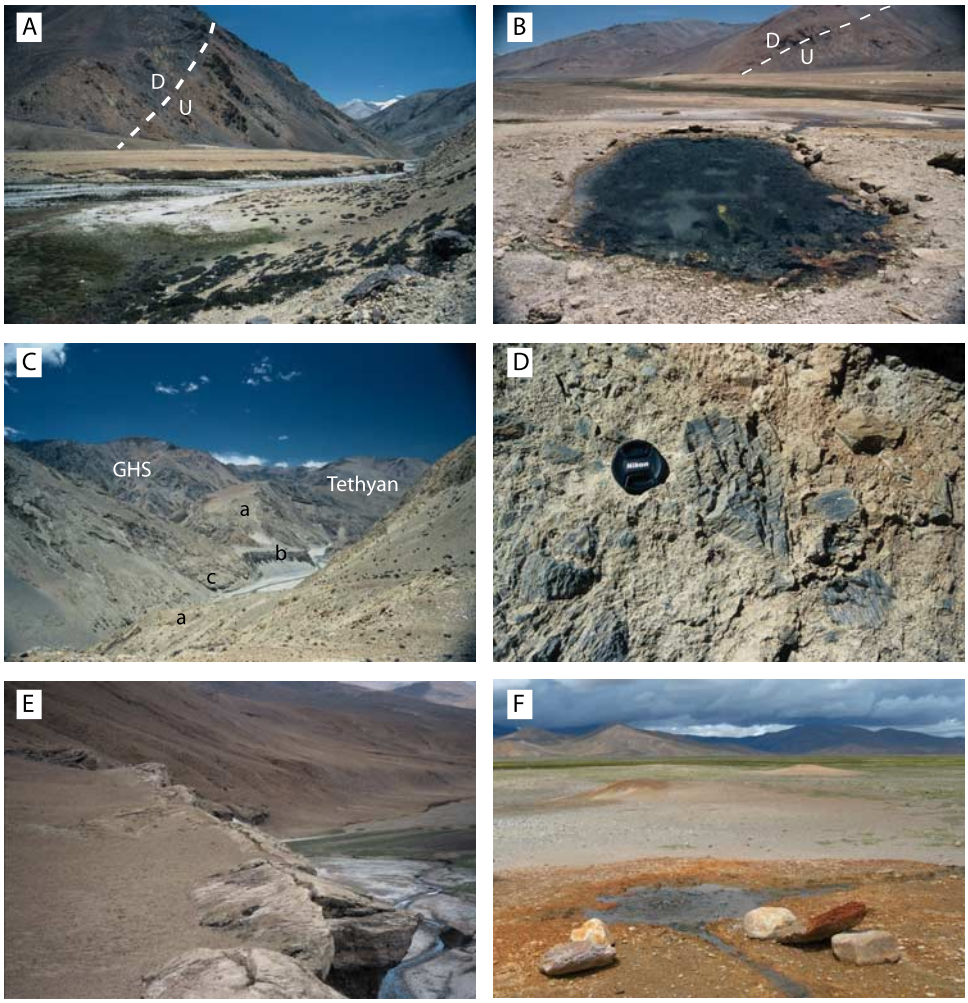

Figure 3. Travertine deposits and mineral springs along the STDS in the Everest region of southern Tibet. Figures 3a and 3b (looking NE) show travertine flowstone terraces and spring mounds found near Nyalam; the trace of the STDS is shown by the dashed line. Carbonate deposits found along the Dzakaa Chu near Kharta (Figure 3c, looking west) include massive cemented breccias (a), cemented river terraces (b), and cemented colluvium (c). The STDS trends east-west, separating sheared marbles of the GHS (Greater Himalayan Series) from the Tethyan Sedimentary Series. Breccia deposits (Figure 3d) composed of sheared marble clasts in a carbonate matrix. Gondasampa warm spring fissure-ridge travertine deposits (Figure 3e, looking south) and bubbling spring mounds (Figure 3f).

the Tingri graben, near the town of Old Tingri (Figure 1). On the west side of the graben, travertines are associated with Tsamda hot springs [*Hoke et al.*, 2000], whereas, to the east side, they are associated with the Gondasampa hot springs. Fissure-ridge and spring-mound travertine deposits [*Chafetz and Folk*, 1984] are present at both locations (Figure 3). Prominent fissure ridges are aligned parallel to the N-S strike of the normal faults: a more localized set of ridges is oriented orthogonal (~080°) to the main fault trace at Tsamda hot spring. Joint sets and minor faults within the TSS are filled with banded carbonate vein deposits. Springs seeps and mounds are numerous at each location ($\gg$10) and are presently degassing (bubbling) with water discharges rates of ~2 l/min. These discharge rates did not vary between the two field campaigns (wet and dry seasons).

3.2. South Tibetan Detachment System (Intermediate Structural Level)

[12] North of Nyalam, travertine deposits are found at two locations along the Bhote Kosi River and one of its unnamed tributaries (Figures 1–3). *Zentmyer et al.* [2008] first described these travertines and identified terraced mounds and cascade deposits that occur at the intersection between the STDS and river valleys. Active springs form constructional mounds of travertine at both locations

as well as numerous small seeps along the base of older travertine deposits. Spring flows ranged from a few l/min to ~500 l/min.

[13] The second zone of carbonate deposition that is representative of this intermediate structural level is present at the intersection of the STDS and the Dzakaa Chu (river), ~100 km east of the Nyalam travertines (Figures 1 and 2). Here, travertine flowstone, together with carbonate-cemented river terraces, colluvial slopes, and massive breccias, are common (Figure 3). River terraces located up and downstream from this zone, however, are not carbonate cemented. Cemented breccias, up to several hundred meters thick, are composed of clasts of sheared marbles from the GHS, and are found along an approximate strike of 250°, similar to the strike of the STDS. Brittle, extensional, low-angle faults (290–21°NE), with slickensides and slickenlines (22°, 354°), offset at least one section of the deposit. Springs issue from beneath carbonate-cemented colluvial slopes and breccia deposits at the level of the Dzakaa Chu and a minor tributary stream. Springs were characterized by high flow rates (~200 l/min) but without a degassing, free gas phase at the time of sampling.

3.3. Ama Drime Massif (Lowest Structural Level)

[14] The ADD on the western limb of the ADM strikes N-S and dips ~25°W beneath the Lhuchung hot springs (Figure 1). Lhuchung hot spring issues from gneisses and leucogranites covered with aggraded river sediments within a small village adjacent to the Dzakaa Chu (Figures 1 and 2). The spring was flowing at ~10 l/min, was not actively degassing (bubbling), and did not have any observable mineral deposits. Nyi Shar hot spring issues from valley alluvium and is located near the northern end of the ADM where the limbs of the antiform merge to form the north-plunging nose of the range (Figure 2). Here, the structure of the range includes a hanging wall block of schist that is overlain by a relatively thin cover of alluvium and underlain by the west-dipping shear zone and gneisses common to the core of the ADM. The spring had a flow rate of ~200 l/min, but was not bubbling gas at its source and had no mineral deposits.

4. Methods

4.1. Water and Gas Sampling

[15] Springs were sampled as close to source outlets as possible during the dry season of 2005 and wet season of 2006. Water samples were collected in 125 mL high-density polyethylene (HDPE) bottles. Samples for alkalinity determination and anion analysis were collected unfiltered with no head-space. Samples for cation analysis were field filtered using 0.45 μm syringe filters and were preserved with concentrated HNO_3.

[16] Gas samples were collected using several techniques developed for sampling volcanic systems, and hot and mineral springs [*Giggenbach and Goguel*, 1989; *Hilton et al.*, 2002]. At actively degassing springs, exsolved gases were collected by submerging a plastic funnel over bubbling regions, allowing the gases to purge the sampling system before drawing them into an evacuated glass Giggenbach bottle. Bottles were used with and without concentrated NaOH; bottles with NaOH were used for concentrating free gases from bubbling springs. At non-bubbling springs, water samples for dissolved gas extraction were also drawn into containers without NaOH [*Giggenbach and Goguel*, 1989].

[17] Samples for He isotope analysis were collected in copper tubes that were sealed with refrigeration clamps. Gas splits for carbon isotope analysis were prepared during the gas purification and extraction of some splits of samples collected for helium isotope samples. Exsolved gases from bubbling springs were sampled for carbon stable isotope analysis using gas displacement into 12 mL glass vials with gas-tight septa caps.

4.2. Sample Analysis

[18] Source temperature, pH and conductivity were measured using an Oakton pH/con 300 portable meter. Anion concentrations in spring waters were analyzed on a Dionex 500X Ion Chromatograph. A Perkin Elmer ICP was used for measuring major cation concentrations. Alkalinity determinations were made by titration.

[19] Gas compositional analysis on sample headspace volumes in Giggenbach bottles was performed at the University of New Mexico Volcanic and Geothermal Fluid Analysis Laboratory on a GOWMAC gas chromatograph to determine N_2, Ar, O_2, H_2, He, CH_4 and CO (and CO_2 for bottles without NaOH) concentrations. For sample bottles collected in NaOH solutions, CO_2 concentrations were determined using wet chemistry (titration) [*Giggenbach and Goguel*, 1989].

[20] The $\delta^{13}C$ of dissolved inorganic carbon (DIC) in water was measured at the University of New Mexico Stable Isotope Laboratory. Spring waters were injected into He flushed glass vials, acidified with 100% H_3PO_4, and allowed to react for 24 h at 25°C prior to analysis. The generated CO_2 was analyzed on a Finnigan Delta Plus isotope ratio mass spectrometer with a Finnigan MAT GASBENCH 2 front-end. The $\delta^{13}C$ of CO_2 bubbling from springs was measured in one of two ways: (1) For purified gas splits prepared during He sample extraction, the samples were run conventionally on a dual-inlet Finnigan Delta XL Plus isotope ratio mass spectrometer; (2) CO_2 collected in 12 mL glass vials was analyzed in continuous flow using a GASBENCH 2 open split interface and a Finnigan Delta Plus mass spectrometer. All carbon results are reported in per mil relative to Peedee belemnite (PDB) with a 1-sigma error of <0.2‰ (defined with NBS-19 = +1.95‰ PDB [*Sharp*, 2006]).

[21] Nitrogen isotope ratios were analyzed at the University of New Mexico Stable Isotope Laboratory using a Finnigan Delta Plus isotope ratio mass spectrometer with a Finnigan MAT GASBENCH 2 interface. Sealed glass sample vials were placed into Swagelok® stainless steel flex tubing sealed with a rubber septum at one end. A two-hole needle was used to pierce the septum and flush the sample chamber with He. When the outer chamber was fully purged of air and no nitrogen peaks were detected on the mass spectrometer, the sample vial was cracked releasing the sample into the entire purged volume. Before beginning an analysis, the chamber was allowed to reach atmospheric pressure because most sample splits were at less than atmospheric pressures. Gas splits were then injected using a 1.0 mL/min He carrier gas and a 100 μL sample loop of a 6-way valve. Results are reported as $\delta^{15}N$ in per mil relative to air with a 1-sigma error of 0.3‰ (air defined as 0.0‰ [*Sharp*, 2006]).

[22] Helium isotope ratios were measured at the Fluids and Volatiles Laboratory at Scripps Institution of Oceanography using procedures described by *Shaw et al.* [2003]. Sample $^3He/^4He$ ratios (R) are reported relative to air (R_A) which has a value of 1.4×10^{-6} [*Graham*, 2002]. These ratios are corrected for air-saturated water dissolved helium (air contribution) using $((R/R_A)X\text{-}1)/(X\text{-}1)$ where X is the air-normalized He/Ne ratio multiplied by β_{Ne}/β_{He}, where β_{Ne} and β_{He} are the Bunsen solubility coefficients for neon and helium in pure water [*Hilton*, 1996] at a temperature of 5°C. Resulting air-corrected values are reported as R_C/R_A (Table 3).

5. Results

5.1. Aqueous and Gas Chemistry

[23] Water chemistry is presented by structural level (see Table 1 and Figure 4). Springs at the highest structural level (Tsamda and Gondasampa) range from 19.2 to 42.6°C, pH 6.34–6.76, and 957–1850 ppm total dissolved solids (TDS). These waters are classified as Na+K-HCO_3 and are saturated with respect to calcite on the basis of calculations using the computer code PHREEQC [*Parkhurst and Appelo*, 1999]. Temperature, pH, specific conductivity and water chemistry did not vary significantly between the dry season (spring) in 2005 and repeat sampling during the summer monsoon season in 2006. Springs located along the STDS range from 7.4 to 20.8°C, pH 6.26–7.68, and 164–978 ppm TDS. These waters are Ca-HCO_3 type, and range from undersaturated to saturated with respect to calcite, and did not vary significantly between the dry and wet seasons of 2005 and 2006, respectively. The hot springs located issuing from the ADD range from 39.9 to 46.8°C, pH 6.85–7.29, and 316–979 ppm TDS. The waters are undersaturated with respect to calcite and are classified as Na+K-HCO_3. These springs were only sampled during the monsoon season of 2006, and no assessment can be made of their inter-annual variability.

[24] Gas composition data are reported in Table 2, and plotted on a He-Ar-N_2 diagram (Figure 5). Gases plotting above the He-N_2/Ar_{air} tie line in Figure 5 have nitrogen in excess of typical meteoric levels. Gases with N_2/Ar ratios greater than 84 (the atmospheric ratio) are considered to have excess nitrogen. The exsolving gases (excluding water vapor) from Tingri graben springs are > 98% by volume CO_2. N_2/He ratios greater than atmospheric levels indicate that gases are a mixture of atmospheric and a crustal/deep-seated source (Figure 5): all samples that plot left of the N_2 – Ar axis contain helium in excess of atmospheric level (excess He). Excess N_2 at Gondasampa spring indicates a mixture of atmospheric and a deep-seated source (Figure 5). Gases exsolving from springs along the STDS near Nyalam range from 56 to 99% CO_2, whereas those issuing from the STDS in the Dzakaa Chu valley have CO_2 concentrations of only 2–3%, the balance being com-

Table 1. Aqueous Chemistry for Tibet Mineral Springs[a]

Sample ID	Name/ Location	T (°C)	pH	TDS (ppm)	F	Cl	Br	NO_3	SO_4	HCO_3	Ca	K	Mg	Na	Saturation Index Calcite[b]
TB-1	Tsamda	42.6	6.3	957	3.07	24.0	0.09	0.09	1.0	1507	120.7	60.4	33.0	337.9	0.13
TS-1	Tsamda	33.7	6.4	1275	3.13	23.8	0.08	0.28	1.9	1538	148.3	59.9	28.1	396.2	0.20
TB-8	Gondasampa	24.5	6.8	1720	5.15	122.8	0.38	8.56	0.7	2343	185.9	133.3	14.1	875.9	0.67
GS-1	Gondasampa	19.2	6.7	1850	4.53	99.5	0.31	0.26	0.1	2258	150.6	96.1	13.0	727.6	0.43
TB-2	Dzakaa Chu	7.9	7.4	229	0.11	0.9	nd	1.30	94.8	168.6	63.9	1.3	21.9	31.61	−0.32
TB-3	Dzakaa Chu	8.2	7.7	164	0.13	2.7	nd	1.53	38.0	130.0	44.9	1.6	9.1	28.28	−0.23
TB-12	Nyalam	7.4	7.6	812	0.20	25.0	0.04	0.22	88.2	1397	357.4	34.2	66.5	97.13	1.4
TB-18	Nyalam	8.1	6.3	253	0.32	0.8	nd	0.02	39.8	207.5	72.2	1.5	13.7	25.15	−1.2
TB-19	Nyalam	20.1	6.6	659	nd	1.4	nd	0.07	66.4	982.4	282.5	5.4	45.7	31.97	0.34
STD-1	Nyalam	20.8	6.5	773	0.32	2.1	nd	0.02	61.6	1046	277.4	5.0	42.3	17.38	0.37
AD-2	Nyi Shar	46.8	6.9	316	7.91	19.3	0.08	0.03	18.7	270.0	17.8	5.8	1.5	115.2	−0.59
AD-1	Lhuchung	39.9	6.2	979	11.04	92.0	0.28	0.04	123.5	887.8	23.6	8.7	1.6	490.0	−0.92

[a] All concentrations reported in mg L^{-1}; nd, not detected.
[b] SI, saturation index defined as the log[ion activity product(IAP)/solubility product(Ksp)]; calculated using PHREEQC [*Parkhurst and Appelo*, 1999].

posed mainly of nitrogen. Excess He and N_2 are found at both locations. Along the ADM, CO_2 content ranges from 1–22%, the balance again being primarily nitrogen. The highest proportion of excess He and N_2 are found at this location. At the Tingri graben and ADM, methane had concentrations of 110 to 500 ppm, but was below detection limits along the STDS.

5.2. He, C, and N Isotope Compositions

[25] Isotopic results are given in Table 3. Air-corrected $^3He/^4He$ ratios from all but one spring

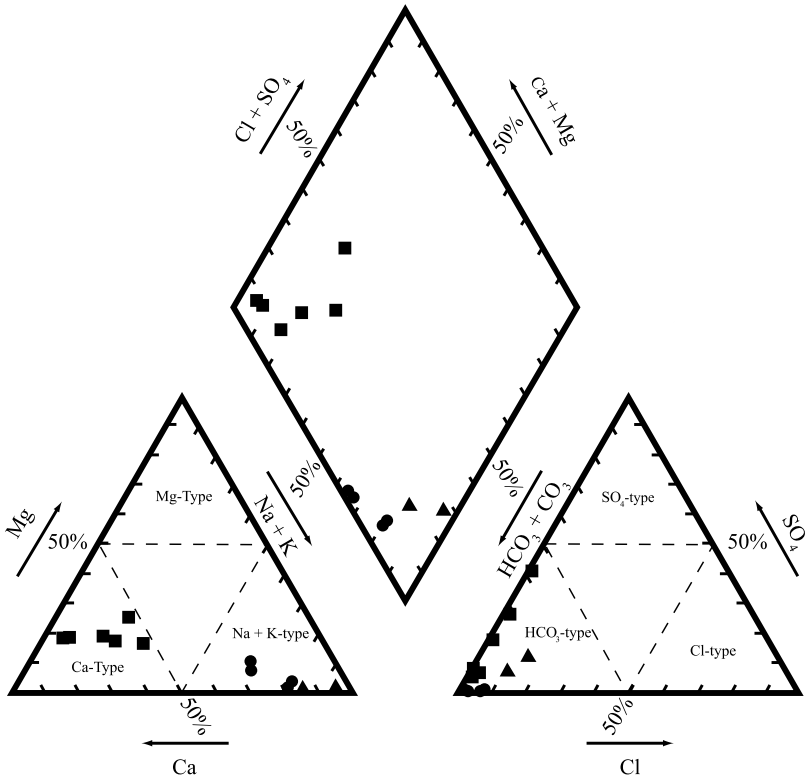

Figure 4. Piper diagram [*Piper*, 1944] plotting major cations in the bottom left, major anions in the bottom right, and a graphical projection of those fields into the parallelogram at top. Solid circles, highest structural level; solid squares, intermediate level; solid triangles, lowest level.

Table 2. Gas Composition for Tibet Mineral Springs[a]

Sample ID	CO_2	He	H_2	Ar[b]	O_2	N_2	CH_4	CO
TB-1	997	0.0039	0.0139	0.026	0.656	2.18	0.1120	<0.0001
TB-8	997	0.0012	0.0030	0.017	1.09	1.38	0.2757	<0.0001
GS-1	986	0.0414	<0.0116	0.051	0.771	12.8	0.4014	<0.0028
TB-2	<32.1	<0.0820	0.5525	15.5	331	621	<0.0197	<0.0197
TB-3	<18.6	0.2741	0.3086	2.9	288	690	<0.0197	<0.0197
TB-12	994	<0.0010	0.0083	0.105	1.90	4.20	<0.0003	<0.0003
TB-19	559	0.4213	0.0086	4.55	60.0	376	0.0127	<0.0010
STD-1	684	0.6381	0.0177	2.45	9.59	303	<0.0027	<0.0027
AD-2	13.2	0.3045	<0.0132	0.63	233	753	0.4967	<0.0033
AD-1	220	13.65	<0.0107	2.85	0.192	763	0.3527	<0.0026

[a] Gases reported as mole fraction in mmol/mol.
[b] Ar values corrected for O_2 interference on the GC.

range from 0.018 to 0.063 R_A. On the basis of high air-normalized He/Ne ratios (45–236,000), air contamination is minor, so that only a small air correction is required (Table 3). Sample TS-1 from Tsamda hot spring has an anomalously high value of 0.98 R_A and a low He/Ne ratio of 3.1, in contrast to previously published values of 0.037 and 0.044 R_A (Table 3) [*Hoke et al.*, 2000]. Sample TS-1 was collected from a man-made hot spring bathing pool, and on the basis of the air-like $^3He/^4He$ value and relatively low He/Ne ratio, helium loss and air introduction in the plumbing system seems probable. The helium isotope result for TS-1 is not considered further, and the published results for the spring are used for comparison.

[26] Carbon isotope ratios for the highest and intermediate structural levels are similar. $\delta^{13}C_{CO2}$ values range from −3.9 to −0.3‰ (versus PDB), with corresponding $\delta^{13}C_{DIC}$ values of 0.4 to +3.8‰ (Figure 6). In contrast, the isotopic ratios from the lower structural level are much lower.

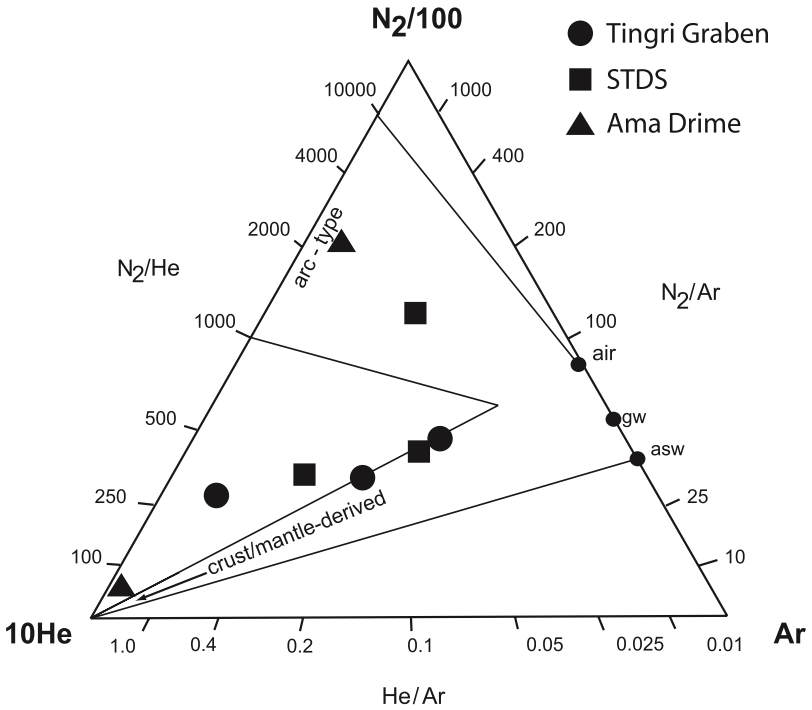

Figure 5. He-Ar-N_2 plot of Tibet mineral spring gases [*Giggenbach et al.*, 1993]. Fields for the crust/mantle, volcanic arcs, air, gw (average groundwater), and asw (air-saturated groundwater) are shown for reference [*Giggenbach et al.*, 1993]. N_2 is divided by 100 and He is multiplied by 10 to provide a visual spread in the data while preserving the actual gas ratios on the axes. Spring gases plot as a mixture between a crustal/mantle and atmospheric source; points lying above the He – N_2/Ar tie line contain excess nitrogen.

Table 3. Helium, Carbon, and Nitrogen Isotope Values for Tibet Mineral Springs[a]

Sample ID	R/R_A	He/Ne (Air)	R_C/R_A[b]	$[He]_c$ cm^3 STP/gH_2O	$CO_2/^3He$ ($\times10^{11}$)	$\delta^{13}C_{DIC}$ ‰ (versus PBD)	$\delta^{13}C_{CO2}$ ‰ (versus PBD)	$\delta^{15}N$ ‰ (versus AIR)
TB-1[c]	0.049, 0.063	81.7, 49.1	0.037, 0.044	~1.0E-07	-	-	−2.5	0.1
TS-1	0.987	3.1	0.980 ± 0.037	-	-	3.1	−3.3	0.1
TB-8	-	-	-	-	-	-	−3.0	−1.6
GS-1	0.023	3674	0.022 ± 0.001	-	-	3.8	−3.9	−2.2
TB-2	-	-	-	-	-	-	−2.7	-
TB-3	0.019	839	0.018 ± 0.002	1.30E-05	1.72 ± 0.12	-	−3.0	0.6
TB-12	-	-	-	-	-	-	−0.6	-
TB-14	-	-	-	-	-	-	−0.3	-
TB-18	0.079	44.9	0.063 ± 0.002	1.10E-06	10.6 ± 0.3	0.4	−1.0	-
TB-19	0.053	89.7	0.046 ± 0.002	5.91E-07	60.6 ± 2.7	-	−2.0	−0.5
STD-1	0.027	756	0.026 ± 0.001	-	-	2.8	−4.7	−0.1
AD-2	0.024	3000	0.024 ± 0.001	-	-	−5.5	−13.1	−2.1
AD-1	0.020	236017	0.020 ± 0.001	-	-	−3.1	−10.0	2.1

[a] The error on $\delta^{13}C$ is 0.2‰; error on $\delta^{15}N$ is 0.3‰. Dash (-), not determined.
[b] Corrected for air-saturated water (ASW) dissolved helium using $(R_C/R_A) = ((R/R_A)X\text{-}1)/(X\text{-}1)$, where X is the air-normalized (He/Ne) ratio multiplied by $\beta_{Ne}/\beta_{He} = 1.2857$ at 5°C [*Ozima and Podosek*, 1983], where β_{Ne} and β_{He} are the Bunsen solubility coefficients for neon and helium in pure water. Likewise, the He concentration is corrected for ASW He using $[He]_c = [He]_{measured} * (X\text{-}1)/X$. Errors are reported at the one sigma level.
[c] Helium isotope values for TB-1 previously reported (Zamda Chuku spring) [*Hoke et al.*, 2000].

$\delta^{13}C_{CO2}$ values for the two hot springs are −13.1 and −10.0‰, paired with $\delta^{13}C_{DIC}$ values of −5.5 and −3.1‰, respectively (Figure 6).

[27] The isotopic composition of dissolved nitrogen ($\delta^{15}N$) is reported for the 2006 sampling season only. There is no obvious relationship between $\delta^{15}N$ value and structural level; $\delta^{15}N$ ranges from −2.2 to +2.1‰ (versus Air) (Table 3).

5.3. Geothermometry

[28] We use water chemistry (Table 1) and cation aqueous geothermometry (Table 4, Na-K-Ca [*Fournier and Truesdell*, 1973], Na-K [*Giggenbach*, 1988], K-Mg [*Giggenbach*, 1988], Si [*Fournier and Rowe*, 1966]) to estimate the temperature of last equilibration of the spring waters. Note, however, that temperature estimates using the Na-K thermometer are considered unreliable for systems precipitating calcite and for equilibration temperatures <200°C [*Fournier and Truesdell*, 1973]. The Na-K-Ca system yields more reliable temperature estimates even in systems containing carbonate bedrock because the relationship between Na, K, and Ca is controlled primarily by equilibration with silicate minerals [*Fournier and Truesdell*, 1973]. Precipitation of large amounts of calcite will impact the reliability of this geothermometer, however. Calcite precipitation lowers the calcium concentration in the water, resulting in higher temperature estimates, but this effect is minimal. For example, even if the equilibrium calcium contents were four times greater than what is measured, the calculated temperatures would increase by only ~10°C. The K-Mg system equilibrates rapidly, and is sensitive to re-equilibration at lower temperatures; it is highly sensitive to mixing of shallow, poorly equilibrated waters resulting in temperature estimates that are too low [*Giggenbach*, 1988]. If the discharge rate is high enough to limit silica loss during cooling as the waters travel to the surface, then the silica geothermometers can yield accurate results. Silica indicators are also highly sensitive to mixing and dilution, which results in underestimation of temperature. All of the described geothermometers are sensitive to the level of water-rock equilibration, mixing along the flow path, and mineral precipitation.

[29] We report a range (minimum to maximum) of equilibration temperatures for each structural level to reflect the variables and uncertainties given above. The Na-K system is not used because all springs other than the lowest structural level (ADM) are associated with travertine, and although the ADM temperatures are close to other indicators, they are less than 200°C. Results that are less than the measured spring temperature are also discarded (Table 4). The likelihood of shallow mixing in low-discharge rate springs (<5 L min^{-1}) with near surface infiltration is high, thus the Si indicators may underestimate temperatures. Spring waters from the high, intermediate, and low structural levels have equilibration temperatures ranging

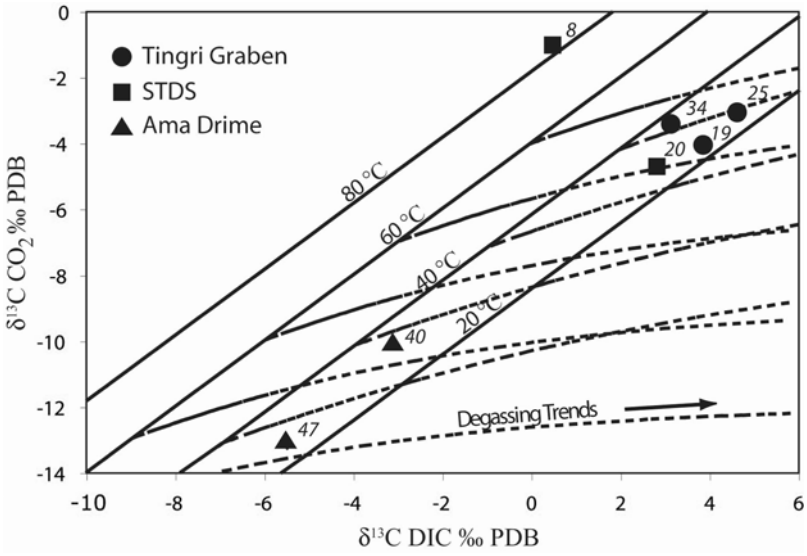

Figure 6. A $\delta^{13}C$ dissolved inorganic carbon (DIC) versus $\delta^{13}C$ CO_2 plot showing paired values for spring waters and exsolving gases. Values reported relative to PDB. Diagonal lines represent temperature-dependent equilibrium relationships between 20 and 80°C. Curves emanating from the 40 and 60°C diagonals represent Rayleigh degassing trends (see text for details). Measured spring temperatures at the time of sampling are shown as italics adjacent to data points.

from 56–215°C, 18–76°C and 47–115°C, respectively (Table 4).

6. Discussion

6.1. Aqueous and Gas Chemistry

[30] Water issuing along the STDS are Ca-HCO_3 type (Figure 4), and all springs observed are associated with accumulations of travertine. Springs issuing from faults in the Tingri graben and along the detachment bounding western limb of the ADM are Na^+K-HCO_3 type (Figure 4). Springs in the Tingri graben are associated with travertine deposits whereas no travertine is associated with the ADM. Also, the springs near the ADM contain a higher percentage of SO_4 + Cl than the Tingri graben. We attribute the variation in water chemistry to differences in rock type that are encountered on fluid flow paths. Springs issuing from the Tingri graben must pass through a thick section of TSS including marine limestone and shale. Springs issuing from the STDS presumably flow along the fault contact between gneiss, schist, leucogranite, and marble of the GHS in the footwall and marine carbonate rocks in the hanging

Table 4. Equilibration Temperatures Based on Geothermometry for Tibet Mineral Springs[a]

Sample ID	Measured	Na^+-K^+	Na^+-K^+-Ca^{2+}	K^+-Mg^{2+}	Silica (Quartz)	Silica (Chalcedony)
TB-1	42.6	283	210	96	–[b]	–[b]
TS-1	33.7	268	201	98	59	27
TB-8	24.5	268	215	131	–[b]	–[b]
GS-1	19.2	255	205	122	56	24
TB-2	7.9	168	10	18	–[b]	–[b]
TB-3	8.2	191	20	30	–[b]	–[b]
TB-12	7.4	358	76	73	–[b]	–[b]
TB-18	8.1	194	10	25	–[b]	–[b]
TB-19	20.1	278	20	37	–[b]	–[b]
STD-1	20.8	333	14	37	20	−13
AD-2	46.8	182	85	76	78	47
AD-1	39.9	124	115	84	84	53

[a] Temperatures reported in °C.
[b] Silica analysis not available for these samples, so a Si temperature cannot be calculated.

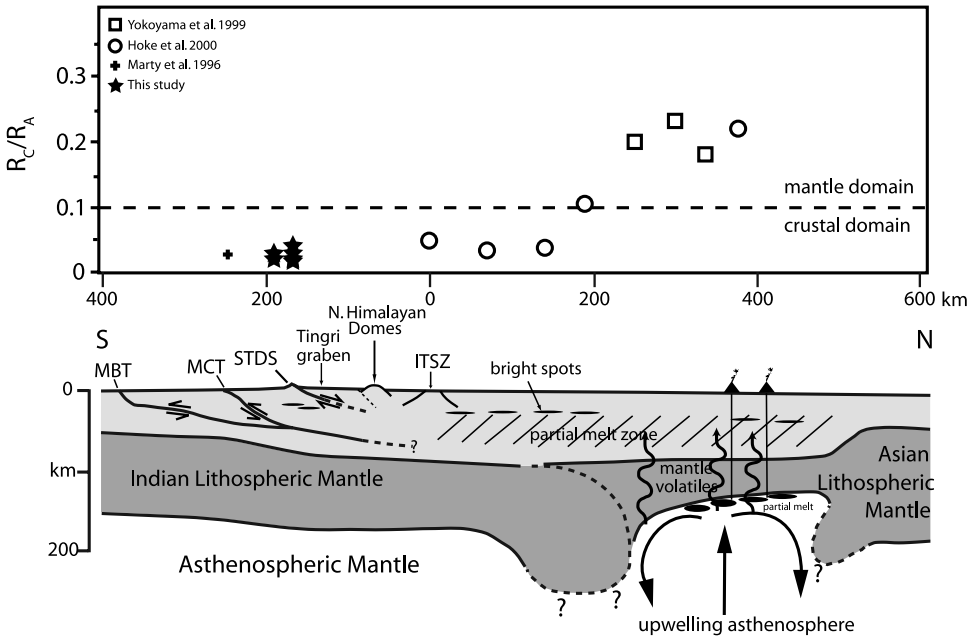

Figure 7. Generalized N–S cross section modified from *Searle et al.* [2003] and *Tilmann et al.* [2003] (with permission from AAAS) with regional $^3He/^4He$ ratios plotted versus N–S distance relative to the Indus-Tsangpo Suture Zone (ITSZ). Data represented by stars, this study; cross, *Marty et al.* [1996]; open circles, *Hoke et al.* [2000]; and open squares, *Yokoyama et al.* [1999]. Seismic bright spots (dark ovals) are interpreted as partial melt and/or fluid rich zones [*Nelson et al.*, 1996]. Ratios are air-corrected (R_C) and reported relative to air (R_A), with the crustal domain defined as $\leq$0.1 R_A and the mantle domain >0.1 R_A.

wall (Figures 2 and 7). Spring waters issuing from the ADM are traveling along the ADD that separates gneiss, schist, and leucogranite of the GHS in the hanging wall from deeper crustal rocks in the footwall block including gneiss, leucogranite and mafic lenses.

[31] The gas chemistry in the springs reflects the mixing of meteoric sources of dissolved gas with those generated within the crust. The types of volatiles present and their relative quantities can be qualitatively tied to the rock types encountered along flow paths. Springs associated with carbonate bedrock, with the exception of those along the STDS in the Dzakaa Chu valley, have the highest CO_2 contents. Springs in the Dzakaa Chu valley, however, do have large carbonate deposits including travertines, cemented river terraces, and cemented colluvium suggesting that elevated CO_2 contents have existed in the recent geologic past. At these two locations, the source of the CO_2 could be decarbonation of these rock types. Springs from the lowest structural level have relatively low CO_2 contents (<22%), and on the basis of surrounding bedrock, the presence of carbonate rocks along the flow paths seems unlikely, so other sources must be invoked. The presence of methane in Tingri graben and ADD springs points to an organic carbon source along these flow paths. Methane could be derived from deeply buried carbon-bearing rocks or it could be produced in the near surface by biogenic CO_2 reduction or organic matter fermentation. The nitrogen and helium concentrations and their variation between springs can be accounted for by mixing meteoric sources and crustal sources, evidenced by excess gas ratios (Figure 5). Excess nitrogen could be from devolatilation of a sedimentary source, a mantle source, or from near-surface microbial processes. Excess helium is either from radiogenic sources in the crust or from the mantle. On the basis of gas composition alone, however, the actual source of these volatiles cannot be uniquely determined requiring evaluation of the isotopic composition (below).

6.2. $^3He/^4He$ Ratios

[32] Continental crust with negligible additions of mantle volatiles has low $^3He/^4He$ ratios of 0.02 to 0.1 R_A, reflecting a strong radiogenic ^4He component with a very low $^3He/^4He$ production ratio in the crust. The upper asthenosphere, as constrained by samples of mid-ocean ridge basalt (MORB), has a $^3He/^4He$ ratio of 8 ± 1 R_A that indicates the presence of primordial ^3He acquired during Earth formation [*Clarke et al.*, 1969; *Graham*, 2002].

Continental lithospheric mantle has a $^3He/^4He$ ratio of ~6 R_A [*Day et al.*, 2005]. $^3He/^4He$ values between 0.1 and the appropriate mantle end-member (i.e., 6 or 8 R_A) are generally interpreted as a mixture of mantle and crustal sources. Lowering of the mantle value occurs by mixing with radiogenic ^4He as fluids move through the crust [*Ballentine and Burnard*, 2002].

[33] Previous helium isotope studies in geothermal springs of the Tibetan Plateau [*Hoke et al.*, 2000; *Yokoyama et al.*, 1999] showed that fluids located between the Banggong and Indus-Tsangpo Suture zone (ITSZ) carry a small percentage of mantle-derived helium (<3%) (Figure 7). South of the ITSZ, fluids carry only crustal helium. *Hoke et al.* [2000] defined mantle and crustal regimes on the basis of helium isotope results (Figure 7). They proposed that mantle volatiles were introduced into the crust from the injection of mantle-derived partial melts derived from the asthenospheric upwelling zone, interpreted to exist beneath the plateau; the influence of mantle fluids diminished to the south until overwhelmed by the crustal helium reservoir (Figure 7). Their most southerly sampling location is the Tsamda hot spring (Figures 1 and 2). Our helium isotopic results show that springs in the southern Tibetan Plateau in the Everest region are tapping fluids dominated by radiogenic helium, confirming the limit of the crustal regime identified by *Hoke et al.* [2000].

6.3. Carbon Isotope Geochemistry

[34] Carbon isotope values are reported for both dissolved inorganic carbon (DIC), (mainly HCO_3^- given a measured pH range of 6.2 to 7.6), and CO_2 degassing from the spring. A temperature-dependent equilibrium fractionation exists between HCO_3^- and CO_2, with a $\Delta^{13}C$ (HCO_3 - CO_2) value of 8.4‰ at 20°C (Figure 6) [*Emrich et al.*, 1970]. Progressive degassing of the isotopically lighter CO_2 fraction causes the remaining dissolved species to become isotopically heavier (i.e., higher values). Changes can be calculated using a Rayleigh distillation equation [e.g., *Sharp*, 2006] (Figure 6):

$$\delta^{13}C_{DIC} = \delta^{13}C_i + \left(1000 + \delta^{13}C_i\right)\left[(1-f)^{(\alpha-1)} - 1\right] \quad (1)$$

$$\delta^{13}C_{CO2} = \left[1000 + \delta^{13}C_i - \left(1000 + \delta^{13}C_i\right)\left[(1-f)^{\alpha}\right] - 1000f\right]/f \quad (2)$$

where $\delta^{13}C_i$ = the initial carbon value prior to phase separation, $\delta^{13}C_{DIC}$ = the instantaneous isotopic value for the dissolved inorganic carbon for a fraction of degassing (f), $\delta^{13}C_{CO2}$ = the isotopic value for the integrated CO_2 leaving the spring for a fraction of degassing, and α is the temperature-dependent fractionation factor. These equations assume equilibrium at all times.

[35] Where possible, we collected paired DIC and CO_2 samples in order to evaluate whether the species were in isotopic equilibrium, and to calculate the initial $\delta^{13}C$ in the spring water prior to effervescence. The initial bulk $\delta^{13}C$ value of the spring water can only be calculated if both the fractionation factor (related to temperature) and fraction of degassing are known. We can estimate the fractionation on the basis of the measured spring temperatures at the time of sampling and the isotopic values for the DIC and CO_2; most of the springs appear to be near equilibrium assuming that some degassing has occurred (Figure 6).

[36] Carbon isotope data demonstrate that the springs in the Tingri graben and along the STDS form a population that is distinctly different from the ADM springs. Metamorphic decarbonation as a source of CO_2 is suggested by initial carbon values for the shallow-crustal and midcrustal levels which overlap with marine carbonate rocks (0 ± 3‰) [*Hoefs*, 1987; *Sano and Marty*, 1995], assuming limited degassing and cooling since phase separation [*Kerrick and Calderia*, 1993; *Kerrick et al.*, 1995]. Initial calculated carbon values for the lowest crustal level (ADM) are considerably lower (−5 to −9‰) and overlap the mantle range (−6 ± 3‰) [*Marty and Jambon*, 1987; *Trull et al.*, 1993] even though the He isotope ratios indicate an absence of mantle-derived helium, the standard tracer for mantle volatiles. North of the Indus-Tsangpo suture zone (ITSZ), CO_2 in hot springs have similar isotopic values to our results and the springs also have mantle-derived helium isotope values leading to a proposed mantle source for the CO_2 [*Yokoyama et al.*, 1999]. However, on the basis of the purely crustal helium found in the ADM springs, we reject mantle-derived CO_2 as the explanation for our carbon isotope values. The origin of these low (mantle-like) values cannot be explained by a simple comparison to know carbon reservoirs, but requires the presence of some reduced carbon in the source rocks. As previously noted, the methane in these springs could be derived from a deep source or by near-surface biogenic processes. In addition to methane production by biogenic fermentation of organic matter (acetic fermentation), CO_2 is also produced. Meth-

ane formed in freshwater systems ranges in carbon isotope composition from −65 to −50‰, and the associated CO_2 could range from −26 to +8‰, depending on the assumed equilibration temperature fractionation factor [*Whiticar et al.*, 1986]. Mixing of this biogenic CO_2 could alter the isotopic composition of the spring DIC. However, methane and CO_2 are formed in equivalent molar concentrations during acetic fermentation, and the concentration of methane in the springs can be used to judge the impact of this mixing. Sample AD-2 has the highest CH_4 to CO_2 ratio (1:26), but even then, fermentation can impact only ∼4% of the dissolved carbon reservoir, so acetic fermentation is not considered as a viable explanation.

[37] The calculated carbon isotope trajectories are valid only if degassing is occurring at or near equilibrium conditions. Non-equilibrium reactions would likely result in lower fractionations than predicted by equilibrium. For one cold spring sample (8°C) along the STDS (Figure 6), the $\Delta^{13}C$ (DIC – CO_2) value corresponds to a temperature of 80°C. Since this suggests that either the spring is not in carbon isotope equilibrium or an analytical error has occurred in one of the measurements, this spring is excluded from the assessment of the carbon source. Calcite precipitation prior to spring emergence could also affect the carbon isotope systematics. Calcite precipitation can lower the $\delta^{13}C$ value of the remaining bicarbonate, but the effect is minor unless large quantities of calcite are precipitated. Some certainly has precipitated, as evidenced by carbonate veins in country rock at the high and intermediate structural levels. However, the amount of vein material observed is insignificant compared to travertine deposits. Also, most springs in the highest and intermediate structural level are super-saturated with respect to calcite suggesting that large quantities have not been precipitated prior to spring emergence (i.e., the waters have not completely dropped their carbonate load). In contrast, the ADD springs (lowest structural level) are undersaturated with calcite, however, no evidence for mineralization was observed within fracture zones in host rocks. This is consistent with the paucity of carbonate minerals in the GHS, which would be necessary to provide the source for a dissolved carbonate load in the springs. Carbonate veins in country at the high and intermediate structural levels are present, indicating some subsurface precipitation; however, the amount is minimal compared to the volumes of travertine present at the surface.

6.4. Nitrogen Isotope Geochemistry

[38] There are three possible subsurface nitrogen sources for hot springs. Mantle and sedimentary nitrogen have $\delta^{15}N$ values of −5 and +5.5‰ (relative to air, defined as 0‰), respectively [*Bebout and Fogel*, 1992; *Bebout*, 1997; *Fischer et al.*, 2002; *Zimmer et al.*, 2004]. Organic matter and natural gas covers a large range from −20 to +20‰, depending on the degree of organic matter maturation [*Hoering and Moore*, 1958; *Inguaggiato et al.*, 2004]. The $\delta^{15}N$ of ammonium in metasedimentary rocks and associated granites has been reported between +5 and +16‰, and interpreted as of biological origin [*Boyd et al.*, 1993; *Boyd and Philippot*, 1998].

[39] The $\delta^{15}N$ of N_2 in this study ranges between −2.2 and +2.1‰ (Table 3). Springs along the STDS and at Tsamda (Tingri graben) cluster within error of the air value (0 ± 0.5‰). Negative values are found at Gondasampa (Tingri graben) and Nyi Shar (ADM), and positive values are found at Lhuchung (ADM). On the basis of existing models for volcanic gases [*Fischer et al.*, 2002; *Zimmer et al.*, 2004], these values indicate mixtures of mantle-, sediment-, and air-derived (meteoric) nitrogen, but this model does not consider the possibility of near surface biogenic sources. The He isotope ratios are consistent with a crustal provenance and mantle sources are unlikely. The negative $\delta^{15}N$ values are therefore most likely explained by a biogenic source. Methane is found in springs with both negative and positive carbon isotope values, but not at springs with an air-like signature. Methane points to an organic source which, as previously discussed, could be generated in the near surface by biogenic organic matter fermentation. Microbial metabolism in the near surface, such as nitrogen fixing and denitrification, would produce N_2 gas isotope values lower than aqueous nitrogen species.

6.5. Implications for Lithospheric Structure and Processes

[40] Linking the geometries of major structures exposed on the southern margin of the Tibetan Plateau with subsurface features identified by geophysical techniques (e.g., Figure 7) is an important challenge in Himalayan tectonics. By integrating our structural interpretations with gas and water geochemistry, we evaluate how the penetration depth of these faults and the composition of the fluids that issue from these conduits elucidate processes occurring today in the Tibetan Plateau.

Table 5. Summary Characteristics and Fluid Source Interpretation for the Three Structural Levels

Structural Level	Host Rocks	Structure	Volatile Source Depth[a]	Probable Volatile Source
Highest	locally derived sediments, limestone and shale (TSS)	graben bounding normal faults (~60° dip)	<8 km	organic matter breakdown and limestone decarbonation
Intermediate	limestone, marble, leucogranite, gneiss, migmatite (TSS and GHS)	STDS (5–20°C dip)	<8 km	limestone/marble decarbonation
Lowest	leucogranite, mafic lenses, gneiss, migmatite (GHS and deeper)	ADD (25–45° dip)	>10 km	metamorphic devolatization of sedimentary protolith; partial melts; mantle (unlikely)

[a] Assuming 50°/km and minimum temperature for devolatization reactions.

Table 5 summarizes the following discussion of the three structural levels investigated.

[41] The N–S striking normal faults bounding the Tingri graben and the west-dipping ADD along the ADM are associated with spring waters that equilibrated at the highest temperatures of this sample suite: therefore, using temperature as a proxy for depth, we interpret these waters as having experienced the deepest circulation. The springs issuing along the STDS near Nyalam indicate equilibration at the lowest temperatures, and thus these are waters that have circulated to the shallowest depths. Variation in circulation depth could simply be related to the dip of the fault zones. Tingri graben normal faults are steeply dipping (~60°E or W) and have the most deeply circulated waters, whereas the fault bounding the ADM dips ~25 to 45°W and waters record moderate circulation depths. In contrast, the STDS dips between 5 and 20°N and has the most shallowly circulated waters. Using temperature as a proxy for depth requires that the geothermal gradient at all the spring locations is similar. Heat flow from the Tibetan crust is high and variable [*Francheteau et al.*, 1984; *Min and Wu*, 1987], so the actual gradient is quite uncertain, and may vary across this study area.

[42] Whereas water chemistry shows the deep circulation of meteoric groundwaters into these fault zones, elevated CO_2 concentrations (compared to atmospheric or soil sources) and excess He and N_2 dissolved in the spring waters indicates inputs from crustal sources. The possible source of these gases, on the basis of their isotopic compositions, could be metamorphic devolatilization of sedimentary source rocks, breakdown of organic material, natural gas, or the mantle. To better evaluate the sources of the volatiles, the isotopic results must be considered in the context of local bedrock geology.

[43] The Tingri graben is bounded and filled by locally derived fluvial sediments and unmetamorphosed marine sedimentary rocks (carbonate and siliciclastic rocks). Gases are dominantly CO_2 with a marine carbonate isotopic signature, with radiogenic (crustal) He, a mix of atmospheric and isotopically low (negative) N_2, and methane. Since the rocks in the graben were not previously metamorphosed, they have the potential to generate volatiles such as CO_2, CH_4 and N_2 during burial diagenesis and metamorphism. Breakdown of organic material contained in the shale during diagenesis and low-grade metamorphism can produce isotopically negative N_2 and methane. Decarbonation of marine limestone explains the high CO_2 concentrations and high $\delta^{13}C$ values. Assuming a minimum temperature of 400°C for metamorphic decarbonation reactions liberating CO_2 [*Ferry*, 1991] and a thermal gradient of 50°C/km [*Min and Wu*, 1987], the CO_2 is derived from a minimum depth of ~8 km.

[44] Along the STDS, rock types also include unmetamorphosed marine limestone, but additionally contain marble, high-grade gneiss and schist, and leucogranite. Gases are dominantly CO_2 with a marine carbon isotope composition, have a crustal He value, and contain atmospheric N_2 but no methane. Metamorphic decarbonation of carbonate rocks best explains the source of CO_2 and its isotopic composition, and suggest that the STDS is tapping depths equivalent or deeper than the normal faults within the Tingri graben (Figure 7). The absence of excess nitrogen and methane relative to air suggest that formation of these gases in the local lithologic package is minimal.

[45] The ADD juxtaposes high-grade metamorphic rocks of the GHS with high-grade metamorphic rocks of a deeper crustal affinity. Rock types include gneiss, schist, amphibolite, migmatite and leucogranite. In contrast to the other structural levels, CO_2 is subordinate to N_2 (Table 2) and has negative $\delta^{13}C$ values. The $\delta^{15}N$ values of dissolved nitrogen are both positive and negative.

Table 6. Carbon Flux Calculations From Tibet Mineral Springs

Spring (Sample ID)	C_{ext}[a] (mol/L)	Discharge (l/min)	Area (m^2)	CO_2 (mol/a)	CO_2 (mol/m^2*a)
Tsamda (TB-1, TS-1)[b]	0.020	2	1	2.1×10^5	2.1×10^4
Gondasampa (TB-8, GS-1)[b]	0.033	2	1	3.5×10^5	3.5×10^4
Dzakaa Chu (TB-2)	0.002	2	1	1.6×10^3	1.6×10^3
Dzakaa Chu (TB-3)	0.001	200	20	1.1×10^5	5.5×10^3
Nyalam (TB-12)	0.013	2	1	1.3×10^4	4.4×10^3
Nyalam (TB-18)	0.002	500	4	5.0×10^5	1.2×10^5
Nyalam (TB-19, STD-1)	0.009	2	3	9.6×10^3	3.2×10^3
Nyi Shar (AD-2)	0.004	200	2	4.3×10^5	2.2×10^5
Lhuchung (AD-1)	0.015	10	6	8.0×10^4	1.3×10^4
Total				1.7×10^6	
Average					1.4×10^5

[a] $C_{ext} = HCO_3 - (Ca + Mg - SO_4)$ [*Chiodini et al.*, 2004].
[b] Values of C_{ext}, discharge, and area are for individual springs; CO_2 flux calculations are based on 10 spring sources.

Methane is present in the springs, and the helium is derived from the crust. The GHS and ADM rocks are being exhumed and experienced peak metamorphic conditions in the Miocene with main metamorphic fabric developed prior to 20 Ma [*Cottle et al.*, 2007]. On the basis of this geologic history and the lack of carbonate bedrock in the region, it seems unlikely that significant volumes of volatile-rich rocks exist at depth today, and long-term storage of metamorphically derived volatiles in this structural setting is unlikely. However, the results of this study require that active devolatilization is occurring at significant depths below the ADM. The most likely sources of CO_2 are crystallizing partial melts and metamorphic devolatilization reactions [*Newton*, 1989]. Oxidation of graphite occurs at ~500°C [*Selverstone*, 2005] equating to at least 10 km, and crustal melts in the Tibetan Plateau are interpreted to lie between 15 and 20 km [*Gaillard et al.*, 2004]. The presence of seismic bright spots, interpreted as partial melt, located ~15 km below the high Himalaya (as shown in Figure 7) support this possibility. Minor graphitic schist was observed inter-layered with marble within the GHS near Kharta. The negative $\delta^{13}C$ values are ambiguous, and although they overlap with the mantle range, the helium isotope results require that carbon is generated from crustal reservoirs. In order to assign a mantle origin to the carbon, and potentially nitrogen, radiogenic production of ^4He would have to be high enough along the fluid flow path to completely overprint the mantle helium signal.

6.6. CO_2 Flux

[46] The total amount of CO_2 generated by deep-seated processes, such as metamorphic decarbonation, oxidation of graphite and magmatic crystallization, can be calculated from the water chemistry by subtracting the CO_2 contribution by near-surface rock-water interaction, such as carbonate mineral dissolution from the total DIC in solution (Table 6) [*Chiodini et al.*, 2004]:

$$C_{ex} = DIC - \left(Ca^{2+} + Mg^{2+} - SO_4^{2-}\right) \quad (3)$$

where all components are in moles/liter and C_{ex} (excess C) represents the deep-seated carbon source and DIC is primarily HCO_3^-. Biological sources could also contribute to the carbon in solution, but on the basis of carbon isotopes, this impact is considered negligible. Calcium and magnesium are subtracted to account for the moles of carbon from the dissolution of carbonates. Sulphate is added to account for calcium addition to solution from dissolution of gypsum, which does not add carbon. This approach assumes that carbonate (calcite and dolomite) is the major source of bedrock-added carbon. Excess carbon is assumed to leave the spring water as CO_2, with the flux from each spring estimated by multiplying C_{ex} by spring discharge (Table 6). Using field estimates for spring discharge (Table 6), the springs in this study have the potential to discharge ~1.7×10^6 mol CO_2 per year to the atmosphere. For comparison, the CO_2 discharge from thermal springs in the Marsyandi Valley of Nepal, along the MCTZ, is estimated at 5.4×10^9 mol a^{-1} [*Becker et al.*, 2008]. That study used a combination of chloride mass balance in the Marsyandi River and Monte Carlo simulations of degassing based on the $\delta^{13}C$ of spring waters and gases.

[47] Our flux estimate is insignificant compared to the estimated amount of CO_2 generated by meta-

morphism during the uplift of the Himalaya during the Cenozoic ($\sim 10^{11}$ mol a^{-1}) [*Kerrick and Calderia*, 1999], or compared to estimates of global subaerial volcanism (10^{12} mol a^{-1}) [*Williams et al.*, 1992]. However, these springs represent only a small fraction of what could be degassing from deeply penetrating structures along the southern margin of the Tibetan Plateau. In the following, we use measurements from individual springs to estimate the minimum and maximum flux from the southern margin of the Tibetan Plateau.

[48] Although scaling the CO_2 discharge from individual springs to regional flux estimates is uncertain, as a minimum estimate, we assume that the frequency of springs across the southern plateau is equivalent to that of the study area. The study area encompasses $\sim$9450 km^2 (135 km $\times$ 70 km) while the southern plateau is $\sim$2600 km long by $\sim$200 km wide (5.2×10^5 km^2). Therefore, multiplying the flux of the study area by a factor of $\sim$55 ($5.2 \times 10^5/9450$) gives, the integrated CO_2 flux estimated at 9.4×10^7 mol a^{-1}.

[49] This minimum value is based on the assumption that all mineral springs in the study area were identified, which is certainly not the case. Second, our calculations assume that CO_2 is being discharged to the atmosphere only at springs. CO_2 is known to discharge diffusely, as evidenced by forest kills proximal to areas of active magmatism [*Farrar et al.*, 1995]. Moreover, it has been found that diffuse CO_2 discharges in non-volcanic regions of Italy are globally significant ($\sim 10^{11}$ mol a^{-1}) [*Chiodini et al.*, 2004]. Thus, it is likely that CO_2 rich fluids are migrating from the crust to the surface along the strike of the STDS, graben normal faults, and the shear zones related to the ADM.

[50] To estimate a maximum flux from the southern plateau, we estimate the diffuse discharge along fault zones, on the basis of the average of calculated spring CO_2 fluxes (Table 6) and the total length of faults in the southern plateau. The average flux from the study springs is $\sim 1.4 \times 10^5$ mol m^{-2} a^{-1}. The length of the STDS is $\sim$2600 km, and the ADM shear zones are 140 km. The total length of graben normal faults in the study area (Figure 1) is at least 300 km, but this only covers about 13% of the southern Tibetan Plateau; therefore, assuming a similar distribution of grabens across the region then there is $\sim$2300 km of graben bounding normal faults. For the purpose of the calculation we assume the fault zone is 1 m wide. Thus, the total length of faults is of the order of $\sim$5000 km which, when multiplied by the average flux (Table 6), gives an estimated total integrated flux of $\sim 7 \times 10^{11}$ mol a^{-1}.

[51] It is critical to emphasize that our estimate has many assumptions, and thus an unknown uncertainty. For example, we assume that the fault zones are 1 m wide. Some of the fault zones observed are distributed zones of deformation up to 100 m or more wide, and others are discrete zones, a meter or less in width. Also, we assume that all faults are tapping regions of elevated CO_2 and serving as conduits to the surface. Finally, we also do not consider CO_2 that may be sequestered for a period of time in shallow aquifers, prior to slow, diffuse degassing to the surface. Our intent here is to present possible limits on fluxes.

[52] *Becker et al.* [2008] acknowledge that their CO_2 flux estimate for the Marsyandi Valley alone is not globally important; however, they scale their estimate to the entire Himalayan arc, giving a total flux of 9×10^{11} mol a^{-1}, which is comparable to our maximum estimate for the southern plateau. *Becker et al.* [2008] scaled their integrated CO_2 flux estimates obtained for the Marsyandi Valley to the total area of the Himalaya. Their estimate is based on flux out of the MCTZ, south of the Himalayan arc, whereas, the flux given here is for the southern plateau, north of the arc. Since both estimates are based on inherently uncertain scaling methods, it is unclear to what extent these estimates overlap, or whether they represent fluxes from two distinct tectonic regions of the Himalaya. Nonetheless, CO_2 discharge values on the order of 10^{11} mol a^{-1}, if accurate, suggest that the Himalayan orogen is an important contributor to the global carbon budget today.

7. Conclusions

[53] This study demonstrates an association between extensional fault zones and CO_2-rich mineral springs along the southern margin of the Tibetan Plateau. $^3He/^4He$ values for these spring waters confirm that the fluid chemistry beneath the southern margin of the Tibetan Plateau is of crustal origin. However, there are distinct differences in crustal provenance between these fluids. Fluids migrating along the N–S trending faults bounding the ADM are communicating with the deepest crustal level, whereas, fluids issuing from the STDS and Tingri graben are associated with shallower crustal levels.

[54] Aqueous and gas geochemistry of mineral springs issuing along major faults can be linked to

flow path rock types and volatile-generating processes within the crust. Faults provide permeable conduits to midcrustal depths, and on the basis of this study, the N-S striking extensional faults cross-cutting the STDS are the most active tectonic features in the southern margin of the Tibetan Plateau. By investigating springs from different structural levels along an E-W transect, we have described orogen-parallel heterogeneities not typically depicted in the traditional N-S view (Figure 7).

[55] Aqueous chemistry records the exchange of deeply circulated meteoric waters with crustal rocks. Gas and isotope chemistry indicates that a variety of processes are generating volatiles deep beneath the Tibetan Plateau today. Metamorphic decarbonation is an important source of CO_2 where carbonate bedrock exists at appropriate depths. Carbonate rocks are absent from the deepest crustal levels investigated (ADM) and isotopic evidence suggest active magmatism (e.g., "bright spots," Figure 7) and metamorphism of metasedimentary rocks containing organic carbon could contribute to the carbon flux. Excess nitrogen can best be explained by metamorphic devolatilization of these rock types or by near-surface biogenic processes. The apparent disconnect between the aqueous and gas tracers is interpreted as a result of mixing of small quantities of deeply derived fluids, high in dissolved gases including CO_2, N_2, and radiogenic He, with higher volume, shallower groundwater. Similar mixing relationships have been identified in mineral springs in the western U.S. [*Crossey et al.*, 2006; *Newell et al.*, 2005].

[56] CO_2 flux estimates based on spring chemistry and discharge range from 9.4×10^7 to 7×10^{11} mol a^{-1}. The upper estimate compares to other globally significant carbon fluxes. This estimate has considerable uncertainties, but nevertheless represents the first estimate of CO_2 flux for the Tibetan Plateau based on field sampling of modern, degassing springs, facilitating comparisons to other estimates for the Himalaya [*Becker et al.*, 2008; *Kerrick and Calderia*, 1993] and other collisional orogens.

Acknowledgments

[57] Funding for this research was provided by a NSF Integrative Graduate Education and Research Traineeship (DGE-9972810), a Geological Society of America Research Grant (Newell), the University of New Mexico Regents Graduate Fellowship (Newell), a Fellowship from the College of Science, Virginia Tech, to M. Jessup, and by a New Zealand TEC Bright Future Top Achiever Doctoral Scholarship (Cottle), the University of New Mexico, Department of Earth and Planetary Sciences Stable Isotope Laboratory (Sharp), and by the NSF EAR-0001133 (Hilton). We thank Sonam Wangdue for his invaluable help in the field, Tashi Sherpa for his logistical support, and Viorel Atudorei (University of New Mexico, Department of Earth and Planetary Sciences) and Mary Ray (Scripps Institution of Oceanography) for their support in stable isotope and helium isotope measurements, respectively. The manuscript benefited greatly from critical reviews from Stuart Gilfillan and an anonymous reviewer.

References

Ballentine, C. J., and P. G. Burnard (2002), Production, release and transport of noble gases in the continental crust, in *Noble Gases in Geochemistry and Cosmochemistry*, *Rev. Mineral. Geochem.*, vol. 47, edited by D. Porcelli et al., pp. 481–538, Mineral. Soc. of Am., Washington, D. C.

Bebout, G. E. (1997), Nitrogen isotope tracers of high-temperature fluid-rock interactions: Case study of the Catalina Schist, California, *Earth Planet. Sci. Lett.*, *151*, 77–90, doi:10.1016/S0012-821X(97)00117-9.

Bebout, G. E., and M. L. Fogel (1992), Nitrogen-isotope compositions of metasedimentary rocks in the Catalina Schist, California: Implications for metamorphic devolatilization history, *Geochim. Cosmochim. Acta*, *56*, 2839–2849, doi:10.1016/0016-7037(92)90363-N.

Becker, J. A., et al. (2008), Himalayan metamorphic CO_2 fluxes: Quantitative constraints from hydrothermal springs, *Earth Planet. Sci. Lett.*, *265*(3–4), 616–629, doi:10.1016/j.epsl.2007.10.046.

Boyd, S. R., and P. Philippot (1998), Precambrian ammonium biogeochemistry: A study of the Moine metasediments, Scotland, *Chem. Geol.*, *144*, 257–268, doi:10.1016/S0009-2541(97)00135-6.

Boyd, S. R., et al. (1993), The measurement of $\delta^{15}N$ in crustal rocks by static vacuum mass spectrometry: Application to the origin of the ammonium in the Cornubian batholith, southwest England, *Geochim. Cosmochim. Acta*, *57*, 1339–1347, doi:10.1016/0016-7037(93)90070-D.

Brown, L. D., et al. (1996), Bright spots, structure, and magmatism in southern Tibet from INDEPTH seismic reflection profiling, *Science*, *274*, 1688–1690, doi:10.1126/science.274.5293.1688.

Burchfiel, B. C., et al. (1992), The south Tibetan detachment system, Himalayan Orogen: Extension contemporaneous with and parallel to shortening in a collisional mountain belt, *Spec. Pap. Geol. Soc. Am.*, 269, 41 pp.

Catlos, E. J., et al. (2002), Records of the evolution of the Himalayan Orogen from in situ Th-Pb ion microprobe dating of monazite: Eastern Nepal and western Garhwal, *J. Asian Earth Sci.*, *20*, 459–479, doi:10.1016/S1367-9120(01)00039-6.

Chafetz, H. S., and R. L. Folk (1984), Travertines: Depositional morphology and the bacterially constructed constituents, *J. Sediment. Petrol.*, *54*(1), 289–316.

Chiodini, G., et al. (2004), Carbon dioxide Earth degassing and seismogenesis in central and southern Italy, *Geophys. Res. Lett.*, *31*, L07615, doi:10.1029/2004GL019480.

Clarke, W. B., et al. (1969), Excess ^3He in the sea: Evidence for terrestrial primordial helium, *Earth Planet. Sci. Lett.*, *6*(3), 213–220, doi:10.1016/0012-821X(69)90093-4.

Cottle, J. M., et al. (2007), Structural insights into the early stages of exhumation along an orogen-scale detachment: The

South Tibetan Detachment System, Dzakaa Chu section, *J. Struct. Geol.*, *29*, 1781–1797, doi:10.1016/j.jsg.2007.08.007.

Crossey, L. J., et al. (2006), Dissected hydrologic system at the Grand Canyon: Interaction between deeply derived fluids and plateau aquifer waters in modern springs and travertine, *Geology*, *34*(1), 25–28, doi:10.1130/G22057.1.

Day, J. M. D., et al. (2005), Absence of a high time-integrated ^{3}He/(U+Th) source in the mantle beneath continents, *Geology*, *33*(9), 733–736, doi:10.1130/G21625.1.

Emrich, K., et al. (1970), Carbon isotope fractionation during the precipitation of calcium carbonate, *Earth Planet. Sci. Lett.*, *8*, 363–371, doi:10.1016/0012-821X(70)90109-3.

Farrar, C. D., et al. (1995), Forest-killing diffuse CO_2 emissions at Mammoth Mountain as a sign of magmatic unrest, *Nature*, *376*, 675–678, doi:10.1038/376675a0.

Ferry, J. M. (1991), Dehydration and decarbonation reactions as a record of fluid infiltration, in *Contact Metamorphism*, *Rev. Mineral. Geochem.*, vol. 26, edited by D. M. Kerrick, pp. 351–393, Mineral. Soc. of Am., Washington, D. C.

Fielding, E. J. (1996), Tibet uplift and erosion, *Tectonophysics*, *260*, 55–84, doi:10.1016/0040-1951(96)00076-5.

Fischer, T., et al. (2002), Subduction and recycling of nitrogen along the Central American margin, *Science*, *297*, 1154–1157, doi:10.1126/science.1073995.

Fournier, R. O., and J. J. Rowe (1966), Estimation of underground temperatures from the silica content of water from hot springs and wet steam wells, *Am. J. Sci.*, *264*, 685–697.

Fournier, R. O., and A. H. Truesdell (1973), An empirical Na-K-Ca chemical geothermometer for natural waters, *Geochim. Cosmochim. Acta*, *37*, 1255–1275, doi:10.1016/0016-7037 (73)90060-4.

Francheteau, J., et al. (1984), High heat flow in southern Tibet, *Nature*, *307*, 32–36, doi:10.1038/307032a0.

Gaillard, F., et al. (2004), Evidence for present-day leucogranite pluton growth in Tibet, *Geology*, *32*(9), 801–804, doi:10.1130/G20577.1.

Giggenbach, W. F. (1988), Geothermal solute equilibria: Derivation of Na-K-Mg-Ca geoindicators, *Geochim. Cosmochim. Acta*, *52*, 2749–2765, doi:10.1016/0016-7037(88)90143-3.

Giggenbach, W. F., and R. L. Goguel (1989), *Methods for the Collection and Analysis of Geothermal and Volcanic Water and Gas Samples*, Chem. Div., Dep. of Sci. and Ind. Res., Petone, New Zealand.

Giggenbach, W. F., et al. (1993), Isotopes of He, and CO_2 and CH_4 contents in gases produced along the New Zealand part of a convergent plate boundary, *Geochim. Cosmochim. Acta*, *57*(14), 3427–3455, doi:10.1016/0016-7037(93)90549-C.

Graham, D. W. (2002), Noble gas isotope geochemistry of mid-ocean ridge and ocean island basalts: Characterization of mantle source reservoirs, in *Noble Gases in Geochemistry and Cosmochemistry*, *Rev. Mineral. Geochem.*, vol. 47, edited by D. Porcelli et al., pp. 481–538, Mineral. Soc. of Am., Washington, D. C.

Hilton, D. R. (1996), The helium and carbon isotope systematics of a continental geothermal system: Results from monitoring studies at Long Valley caldera (California, USA), *Chem. Geol.*, *127*(4), 269–295, doi:10.1016/0009-2541(95)00134-4.

Hilton, D., et al. (2002), Noble gases and volatile recycling at subduction zones, in *Noble Gases in Geochemistry and Cosmochemistry*, *Rev. Mineral. Geochem.*, vol. 47, edited by D. Porcelli et al., pp. 319–370, Mineral. Soc. of Am., Washington, D. C.

Hodges, K. V. (2000), Tectonics of the Himalaya and southern Tibet from two perspectives, *Geol. Soc. Am. Bull.*, *112*, 324–350, doi:10.1130/0016-7606(2000)112<0324: TOTHAS>2.3.CO;2.

Hoefs, J. (1987), *Stable Isotope Geochemistry*, 3rd ed., 241 pp., Springer, New York.

Hoering, T. C., and H. E. Moore (1958), The isotopic composition of the nitrogen in natural gases and associated crude oils, *Geochim. Cosmochim. Acta*, *13*, 225–232, doi:10.1016/0016-7037(58)90024-3.

Hoke, L., et al. (2000), Southern limit of mantle-derived geothermal helium emissions in Tibet: Implications for lithospheric structure, *Earth Planet. Sci. Lett.*, *180*, 297–308, doi:10.1016/S0012-821X(00)00174-6.

Hurtado, J. M., et al. (2001), Neotectonics of the Thakkhola Graben and implications for recent activity on the South Tibetan fault system in the central Nepal Himalaya, *Geol. Soc. Am. Bull.*, *113*, 222–240, doi:10.1130/0016-7606(2001)113<0222:NOTTGA>2.0.CO;2.

Inguaggiato, S., et al. (2004), Nitrogen isotopes in thermal fluids of a forearc region (Jalisco Block, Mexico): Evidence for heavy nitrogen from continental crust, *Geochem. Geophys. Geosyst.*, *5*, Q12003, doi:10.1029/2004GC000767.

Jessup, M. J., et al. (2006), Structural evolution and vorticity of flow during extrusion and exhumation of the Greater Himalayan Slab, Mount Everest Massif, Tibet/Nepal: Implications for orogen-scale flow partitioning, *Geol. Soc. Am. Spec. Publ.*, *268*, 379–413.

Jessup, M. J., et al. (2008), Orogen-parallel extension and exhumation enhanced by denudation in the trans-Himalayan Arun River gorge, Ama Drime Massif, Tibet-Nepal, *Geology*, *36*(7), 587–590, doi:10.1130/G24722A.1.

Kerrick, D. M. (2001), Present and past nonanthropogenic CO_2 degassing from the solid Earth, *Rev. Geophys.*, *39*(4), 565–585, doi:10.1029/2001RG000105.

Kerrick, D. M., and K. Calderia (1993), Paleoatmospheric consequences of CO_2 release during early Cenozoic regional metamorphism in the Tethyan orogen, *Chem. Geol.*, *108*, 201–230, doi:10.1016/0009-2541(93)90325-D.

Kerrick, D. M., and K. Calderia (1994), Metamorphic CO_2 degassing and early Cenozoic paleoclimate, *GSA Today*, *4*(3), 62–65.

Kerrick, D. M., and K. Calderia (1999), Was the HImalayan Orogen a climatically significant coupled source and sink for atmospheric CO_2 during the Cenozoic?, *Earth Planet. Sci. Lett.*, *173*(3), 195–203, doi:10.1016/S0012-821X(99)00229-0.

Kerrick, D. M., et al. (1995), Convective hydrothermal CO_2 emission from high heat flow regions, *Chem. Geol.*, *121*, 285–293, doi:10.1016/0009-2541(94)00148-2.

Kind, R., et al. (2002), Seismic images of crust and upper mantle beneath Tibet: Evidence for Eurasian plate subduction, *Science*, *298*, 1219–1221, doi:10.1126/science.1078115.

Law, R. D., et al. (2004), Strain, deformation temperatures and vorticity of flow at the top of the Greater Himalayan Slab, Everest Massif, Tibet, *J. Geol. Soc.*, *161*, 305–320, doi:10.1144/0016-764903-047.

Makovsky, Y., and S. L. Klemperer (1999), Measuring the seismic properties of Tibetan bright spots: Evidence for free aqueous fluids in the Tibetan middle crust, *J. Geophys. Res.*, *104*(B5), 10,795–10,825, doi:10.1029/1998JB900074.

Marty, B., and A. Jambon (1987), C/^{3}He in volatile fluxes from the solid Earth: Implications for carbon geodynamics, *Earth Planet. Sci. Lett.*, *70*, 196–206.

Marty, B., et al. (1996), CO_2 and helium in mineral springs of Nepal and Mustang: A study of volatile release processes during the Himalayan tectonics, paper presented at 11th Himalayan-Karakorum-Tibet Workshop, Northern Ariz. Univ., Flagstaff, Ariz.

Min, Z., and F. T. Wu (1987), Nature of the upper crust beneath central Tibet, *Earth Planet. Sci. Lett.*, *84*, 204–210, doi:10.1016/0012-821X(87)90086-0.

Nelson, K. D., et al. (1996), Partially molten middle crust beneath southern Tibet: Synthesis of Project INDEPTH results, *Science*, *274*, 1684–1688, doi:10.1126/science.274.5293.1684.

Newell, D. L., et al. (2005), Continental-scale links between the mantle and groundwater systems of the western United States: Evidence from travertine springs and regional He isotope data, *GSA Today*, *15*(12), 4–10, doi:10.1130/1052-5173(2005)015[4:CSLBTM]2.0.CO;2.

Newton, R. C. (1989), Metamorphic fluids in the deep crust, *Annu. Rev. Earth Planet. Sci.*, *17*, 385–412, doi:10.1146/annurev.ea.17.050189.002125.

Ozima, M., and F. Podosek (1983), *Noble Gas Geochemistry*, 377 pp., Cambridge Univ. Press, Cambridge, U. K.

Parkhurst, D. L., and C. A. J. Appelo (1999), User's guide to PHREEQC (Version 2)—A computer program for speciation, batch-reaction, one-dimensional transport, and inverse geochemical calculations, *U.S. Geol. Surv. Water Resour. Invest. Rep., 99-4259*, 310 pp.

Piper, A. M. (1944), A graphical procedure in the geochemical interpretation of water analyses, *Eos Trans. AGU*, *25*, 914–923.

Sano, Y., and B. Marty (1995), Origin of carbon in fumarolic gas from island arcs, *Chem. Geol.*, *119*, 265–274, doi:10.1016/0009-2541(94)00097-R.

Searle, M. P., et al. (2003), The structural geometry, metamorphic and magmatic evolution of the Everest massif, High Himalaya of Nepal-South Tibet, *J. Geol. Soc.*, *160*, 345–366, doi:10.1144/0016-764902-126.

Selverstone, J. (2005), Preferential embrittlement of graphitic schists during extensional unroofing in the Alps: The effect of fluid composition on rheology in low-permeability rocks, *J. Metamorph. Geol.*, *23*, 461–470, doi:10.1111/j.1525-1314.2005.00583.x.

Sharp, Z. D. (2006), *Principles of Stable Isotope Geochemistry*, 344 pp., Prentice-Hall, Upper Saddle River, N. J.

Shaw, A. M., et al. (2003), Contrasting volatile systematics of Nicaragua and Costa Rica: Insights to C-cycling through subduction zones, *Earth Planet. Sci. Lett.*, *214*(3–4), 499–513, doi:10.1016/S0012-821X(03)00401-1.

Tilmann, F., et al. (2003), Seismic imaging of the downwelling Indian lithosphere beneath central Tibet, *Science*, *300*, 1424–1427, doi:10.1126/science.1082777.

Trull, T., et al. (1993), C-He systematics in hotspot xenoliths: Implications for mantle carbon contents and carbon recycling, *Earth Planet. Sci. Lett.*, *118*, 43–64, doi:10.1016/0012-821X(93)90158-6.

Turner, S., et al. (1993), Timing of Tibetan uplift constrained by analysis of volcanic rocks, *Nature*, *364*, 50–54, doi:10.1038/364050a0.

Wei, W., et al. (2001), Detection of widespread fluids in the Tibetan crust by magnetotelluric studies, *Science*, *292*, 716–718, doi:10.1126/science.1010580.

Whiticar, M. J., et al. (1986), Biogenic methane formation in marine and freshwater environments: CO_2 reduction vs. acetate fermentation—Isotope evidence, *Geochim. Cosmochim. Acta*, *50*, 693–709, doi:10.1016/0016-7037(86)90346-7.

Williams, S. N., et al. (1992), Global carbon dioxide emission to the atmosphere by volcanoes, *Geochim. Cosmochim. Acta*, *56*(4), 1765–1770, doi:10.1016/0016-7037(92)90243-C.

Yokoyama, T., et al. (1999), Helium and carbon isotopic compositions of hot spring gases in the Tibetan Plateau, *J. Volcanol. Geotherm. Res.*, *88*, 99–107, doi:10.1016/S0377-0273(98)00108-5.

Zentmyer, R., et al. (2008), Travertine deposits from along the South Tibetan Fault System near Nyalam, Tibet, *Geol. Mag.*, doi:10.1017/S0016756808005323, in press.

Zimmer, M. M., et al. (2004), Nitrogen systematics and gas fluxes of subduction zones: Insights from Costa Rica arc volatiles, *Geochem. Geophys. Geosyst.*, *5*, Q05J11, doi:10.1029/2003GC000651.